How to cite: *Angew. Chem. Int. Ed.* **2025**, e202508224
doi.org/10.1002/anie.202508224

Lithium Metal Batteries

Titanium–Polyoxometalate Crosslinked Metallo–Supramolecular Polymer as Artificial Interfacial Layer for Highly Persistent and Low–Temperature Tolerant Lithium Metal Batteries

Yaoda Wang[+], Pei-Chen Zhao[+], Jingjie Sun, Junchuan Liang, Tianyu Shen, Cheng-Hui Li, and Zhong Jin**

Abstract: The uncontrolled lithium (Li) dendrite growth and fragile native solid electrolyte interphase formation have severely hindered the practical development of Li metal batteries. Herein, a coordinatively cross-linked metallo-supramolecular polymer as anodic interfacial protective layer (MSP-IPL) is developed by utilizing titanium(IV)–polyoxometalates (Ti-POMs) as hexatopic linkers to bridge organic and inorganic moieties. The constructed MSP-IPL possesses high electrochemical stability, superior ion-transfer ability, and good air stability. Due to its high film formation uniformity and mechanical tenacity, the MSP-IPL can effectively avoid nonuniform Li deposition caused by the tip effect, thus inhibiting Li dendrite proliferation. The uniformly distributed Ti-POMs in polymer skeleton can efficiently bind with PF_6^- anions, thus increasing Li^+ transference number and promoting homogeneous Li^+ distribution. The reprocessability and self-healing ability endowed by dynamic coordination bonds enable the MSP-IPL to accommodate electrode volume changes and maintain good interface contact. Consequently, high-loading Li||$LiFePO_4$ and Li||$LiNi_{0.8}Co_{0.1}Mn_{0.1}O_2$ batteries based on MSP-IPL-coated Li anodes demonstrate impressive cyclability and extraordinary rate capability. Even at a low temperature of −20 °C, the MSP-IPL-coated Li||NCM811 batteries can still cycle stably for over 500 cycles (equivalent to 138 days) with a considerable capacity retention of 86.8%. This work presents a promising solution for developing practical low-temperature Li metal batteries.

Introduction

To meet the ever-growing energy density requirement, it is urgent to develop new high-specific-energy and high-safety rechargeable batteries to replace the traditional lithium-ion batteries.[1,2] Among numerous anode candidates, lithium (Li) metal is considered one of the ultimate choices due to its ultrahigh theoretical capacity (3860 mAh g^{-1} or 2061 mAh cm^{-3}) and ultralow redox electrochemical potential (−3.04 V versus standard hydrogen electrode, SHE).[3,4] However, the practical application of Li metal anodes (LMAs) is considerably restricted by several inherent issues, including the formation of fragile native solid electrolyte interphase (SEI), the uncontrollable Li dendrite nucleation and growth, and the resulting severe safety hazards.[5–8] These problems will be further exacerbated under practical working conditions such as fast charge–discharge and high operating voltage.[9] Therefore, it is critical to develop artificial interfacial layers to replace the native SEI for stable operation of Li metal batteries. To date, various artificial interfacial layers, including inorganic materials[10–15] and organic polymers,[16–19] have been constructed on the LMA surface to improve its compatibility with electrolytes. However, the vast majority of artificial interfacial layers struggle to meet all the desirable requirements simultaneously.[20–22] It is crucial to construct a full-featured artificial interfacial layer that is chemically inert, highly Li-conducting, and mechanically robust to overcome the thorny problems of LMAs.

Incorporating metal–organic coordination structures into polymers as cross-linkages has been demonstrated to effectively upgrade the overall properties of polymer materials.[23] Benefiting from their superior self-recovery capability and tunable bond strength, metal–organic coordination bonds can endow polymers with dynamic and reversible mechanical properties.[24,25] Moreover, due to the unique electronic and stereochemical properties of metal–organic complexes, the polymers cross-linked by metal–organic coordination structures (defined as metallo-supramolecular polymer) can achieve additional functionalities (including conducting, redox, and catalytic properties) by reasonably selecting and combining metal ions and functional organic ligands.[26–28]

[*] Y. Wang[+], P.-C. Zhao[+], J. Sun, J. Liang, T. Shen, Prof. C.-H. Li, Prof. Z. Jin
State Key Laboratory of Coordination Chemistry, MOE Key Laboratory of Mesoscopic Chemistry, MOE Key Laboratory of High Performance Polymer Materials and Technology, Jiangsu Key Laboratory of Advanced Organic Materials, Suzhou Key Laboratory of Green Intelligent Manufacturing of New Energy Materials and Devices, Tianchang New Materials and Energy Technology Research Center, Institute of Green Chemistry and Engineering, School of Chemistry and Chemical Engineering, Nanjing University, Nanjing, Jiangsu 210023, P.R. China
E-mail: chli@nju.edu.cn
zhongjin@nju.edu.cn

[+] Both authors contributed equally to this work.

Additional supporting information can be found online in the Supporting Information section

Consequently, metallo-supramolecular polymers are promising candidate materials for constructing artificial interfacial layers, with the potential to simultaneously meet all the requirements of high chemical stability, excellent mechanical properties, and high ionic conductivity.

Herein, we meticulously design and synthesize an advanced metallo-supramolecular polymer by using a titanium(IV)–polyoxometalate (Ti-POM) as a coordination cross-linking unit and utilize it to prepare a functional metallo-supramolecular polymer interfacial protective layer (MSP-IPL) for stabilizing LMAs. The constructed MSP-IPL possesses superior electrochemical stability and high ion-transfer ability and can effectively prevent gas permeation to ensure the improved stability of LMAs in ambient air. The uniformly distributed Ti-POMs in polymer skeleton are demonstrated to effectively bind with the PF_6^- anions, thereby significantly enhancing Li^+ transference number ($t_{Li}^+ = 0.607$), promoting uniform distribution of Li^+ flux, and inhibiting the growth of Li dendrites. Due to its high film-formation uniformity and mechanical tenacity, the coated MSP-IPL can efficiently avoid nonuniform Li deposition caused by the tip effect, further facilitating dendrite-free Li electrodeposition. Moreover, the reprocessability and self-healing ability endowed by dynamic coordination bonds enable the MSP-IPL to adapt to electrode volume changes and maintain good interfacial contact. Consequently, the high-loading Li||$LiFePO_4$ (LFP, ~2.4 mAh cm^{-2}) batteries based on MSP-IPL-coated Li anodes demonstrate a markedly prolonged cycling lifespan for over 600 cycles at 1.0 C. When assembled with high-loading $LiNi_{0.8}Co_{0.1}Mn_{0.1}O_2$ (NCM811, ~3.0 mAh cm^{-2}) cathodes, the MSP-IPL-coated Li||NCM811 batteries can cycle stably for over 480 cycles with a high-capacity retention of 84.0%. Even at a low temperature of −20 °C, the Li||NCM811 batteries based on MSP-IPL-coated Li anodes still perform competitively, delivering a considerable capacity retention of 86.8% after 500 cycles (equivalent to over 138 days). This study demonstrates the huge potential of coordinatively cross-linked metallo-supramolecular polymer as interfacial protective layer in developing highly durable and dendrite-free Li metal batteries.

Results and Discussion

Rationally designing molecular structure of metallo-supramolecular polymer based on coordinatively cross-linking strategy is crucial for achieving the comprehensive functionality of MSP-IPL. In this study, we synthesized a Ti-POM, hexakis(μ_3-oxo)-hexakis(μ_2–4-aminobenzoato-*O*, *O*')-hexakis(isopropoxy)-hexa-titanium isopropanol solvate (denoted as Ti_6(HPAB)), as a hexatopic linker for metallo-supramolecular polymer preparation owing to its dynamic and tunable Ti─O coordination bonds and appropriate electrostatic interactions with anions in electrolytes. The synthesis process of Ti_6(HPAB) was presented in Scheme S1, and the molecular structure of Ti_6(HPAB) was confirmed by proton nuclear magnetic resonance (^{1}H NMR) and ^{13}C NMR (Figures S1 and S2). By utilizing Ti_6(HPAB) to coordinatively cross-link polyetheramine (M_n~2000, PEA) and isophorone diisocyanate (IPDI), the targeted metallo-supramolecular polymer (denoted as Ti-PEA-IPDI) was synthesized controllably (Figure 1a and Scheme S2). The molecular structure of Ti-PEA-IPDI was demonstrated by ^{1}H NMR and attenuated total reflectance-Fourier transform infrared (ATR-FTIR) spectroscopy (Figures S3 and 1b). For the FT-IR spectrum of Ti-PEA-IPDI, the newly emerged absorption peaks were detected at around 3360, 1640, and 1560 cm^{-1}, corresponding to the N─H stretching vibrations, the C═O stretching vibrations, and the N─H bending vibrations within the urea linkage structure, respectively, confirming the formation of urea linkages and the occurrence of polymerization reaction. Furthermore, the simple synthesis process of Ti-PEA-IPDI and the low costs of required reagents make it promising for large-scale commercialization (Table S1).

Compared with the XRD spectrum of Ti_6(HPAB), the disappearance of XRD diffraction peaks for Ti-PEA-IPDI metallo-supramolecular polymer indicated its amorphous nature (Figure S4), which is favorable to fast Li^+ migration. The similar conclusion can be drawn from investigating the thermal transition of Ti-PEA-IPDI metallo-supramolecular polymer by differential scanning calorimetry (DSC). The glass transition temperature (T_g) of Ti-PEA-IPDI metallo-supramolecular polymer was as low as −55.6 °C (Figure S5), implying its potential in accelerating Li^+ transfer. To investigate the thermal stability of Ti-PEA-IPDI metallo-supramolecular polymer, the thermogravimetric analysis (TGA) measurement was conducted (Figure S6), and the test results demonstrated that the initial decomposition temperature of Ti-PEA-IPDI metallo-supramolecular polymer was up to 310 °C, indicating its feasibility under high-temperature conditions. Furthermore, a series of mechanical performance tests targeting Ti-PEA-IPDI metallo-supramolecular polymer were also conducted to evaluate its mechanical stability as an interfacial protective layer. An ideal interfacial protective layer for Li metal anodes generally requires superior mechanical properties to ensure structural integrity, accommodate electrode volume fluctuations, and effectively suppress Li dendrite growth to some extent.[29–31] Tensile stress–strain curves under different strain rates indicated that the Ti-PEA-IPDI metallo-supramolecular polymer could provide sufficient mechanical strength and toughness to suppress Li dendrite growth (Figure S7). The repeated tensile tests after different crack-healing cycles proved that the Ti-PEA-IPDI metallo-supramolecular polymer possessed superior reprocessability and self-healing ability to accommodate volume changes of LMAs and promptly repair damaged areas (Figure S8). The oscillatory temperature, frequency, and strain sweep experiments obtained via rheological measurement further illustrated that the Ti-PEA-IPDI metallo-supramolecular polymer possessed prominent mechanical stability, protecting LMAs for a long-term stable operation (Figures S9–S11).

The Ti-PEA-IPDI MSP-IPL-coated Li electrodes (denoted as MSP-IPL@Li) were fabricated by a simple and convenient drop-casting method. Briefly, a certain amount of solution composed of Ti-PEA-IPDI metallo-supramolecular polymer in anhydrous *N*-methylpyrrolidone

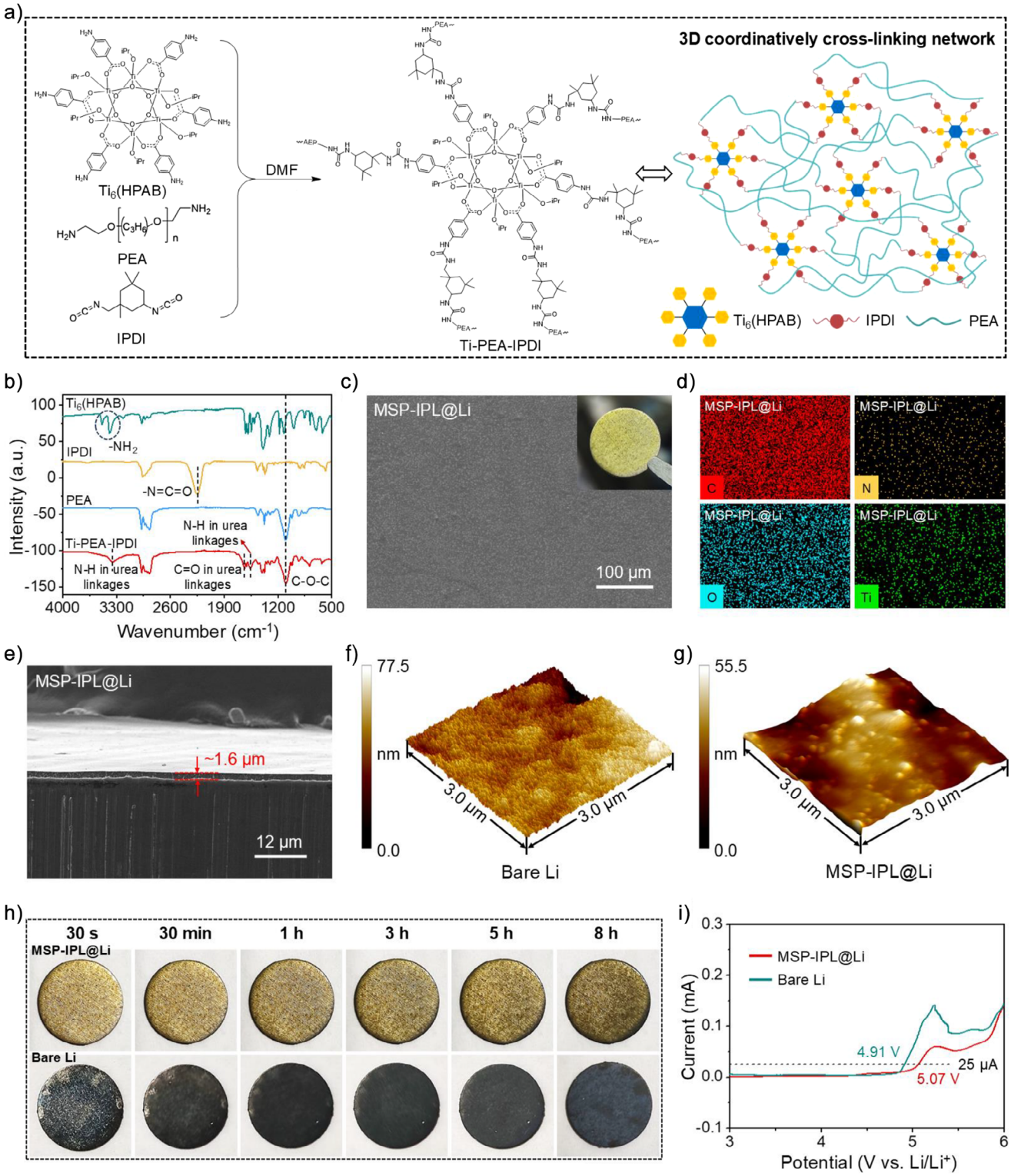

Figure 1. Synthesis route of Ti-PEA-IPDI metallo-supramolecular polymer and characterizations of MSP-IPL@Li. a) Schematic synthesis process and molecular structure of Ti-PEA-IPDI metallo-supramolecular polymer. b) FT-IR spectra of Ti_6(HPAB), IPDI, PEA, and Ti-PEA-IPDI metallo-supramolecular polymer. c) Top-view SEM image of MSP-IPL@Li. Inset: digital image of MSP-IPL@Li. d) Corresponding EDX elemental mappings of C, N, O, and Ti elements on the MSP-IPL@Li. e) Cross-section SEM image of MSP-IPL@Li, showing a uniform thickness of 1.6 μm for the MSP-IPL. AFM topography images of f) bare Li and g) MSP-IPL@Li. h) Air stability test for the MSP-IPL@Li and bare Li. Both electrodes were monitored for various durations after exposure to ambient air with a relative humidity of ~60%. i) LSV curves of MSP-IPL@Li and bare Li based on Li||carbon-coated Al foil batteries at a scan rate of 0.5 mV s^{-1}.

(NMP) was uniformly dropped onto the Li metal surface, and the MSP-IPL@Li was obtained after solvent evaporation. By comparing the Fourier transform infrared (FT-IR) spectrum of MSP-IPL@Li with that of Ti-PEA-IPDI metallo-supramolecular polymer (Figure S12), it was confirmed that the NMP solvent had completely evaporated without weakening the protective effect of MSP-IPL. The surface morphology of the prepared MSP-IPL@Li was investigated via scanning electron microscope (SEM) characterization. For the bare Li (Figure S13), the scraper polishing process exhibited the limited effectiveness in reducing surface roughness, whereas the MSP-IPL@Li presented a flat and smooth surface morphology (Figure 1c). The EDX elemental mappings of MSP-IPL@Li also showed a uniform distribution of C, N, O, and Ti elements (Figures 1d and S14), illustrating that the constructed MSP-IPL was homogeneous and defect-free. SEM technique was also used to monitor the cross-section morphology of MSP-IPL@Li. The SEM image and corresponding elemental mapping images revealed that the MSP-IPL, with a uniform thickness of ~1.6 μm, tightly adhered onto the Li metal surface (Figures 1e and S15). Atomic force microscopy (AFM) analysis was employed to further investigate the difference in surface flatness of MSP-IPL@Li and bare Li. Compared with the rough topography of bare Li (Figure 1f), the AFM topography image of MSP-IPL@Li exhibited markedly improved surface smoothness (Figure 1g). This indicated that the constructed MSP-IPL could efficiently eliminate the original protrusions on the bare Li surface, thus avoiding nonuniform Li deposition caused by the tip effect.

The surface chemical composition of MSP-IPL@Li was probed by X-ray photoelectron spectroscopy (XPS) analysis. The Ti 2p spectrum exhibited a pair of characteristic peaks corresponding to Ti—O species,[32] which was also detected in the O 1s spectrum (Figure S16a,b), demonstrating the existence of Ti—O coordination bonds in the polymer skeleton. For the C 1s and N 1s spectra (Figure S16c,d), a typical characteristic peak assigned to C—N species was detected, indicating the occurrence of polymerization reaction and the formation of urea linkages during the polymerization process. Notably, the Li 1s spectrum of MSP-IPL@Li revealed an absence of Li-containing species (Figure S16e), illustrating the constructed MSP-IPL was dense and chemically inert, ensuring the chemical stability of LMAs. To further highlight the compactness of the constructed MSP-IPL, the difference in air stability of MSP-IPL@Li and bare Li was compared. After exposed to air atmosphere with relative humidity of ~60% (Figure 1h), the color of bare Li completely turned to black within a few minutes. In comparison, no obvious change in color or volume was observed for the MSP-IPL@Li even after exposure to air for 8 h, indicating that the MSP-IPL as a physical barrier could effectively prevent gas permeation and protect the underneath Li metal from air attack. Furthermore, the electrochemical stability of the constructed MSP-IPL was investigated by measuring linear sweep voltammetry (LSV) curves of MSP-IPL@Li (Figure 1i). Compared with the bare Li (~4.91 V), the MSP-IPL@Li exhibited a wider electrochemical stability window (>5.07 V), illustrating that the MSP-IPL@Li could be well compatible with high-voltage cathodes to achieve the construction of high-energy-density Li metal batteries.[16]

To study the effect of MSP-IPL on the initial Li electroplating behavior, the cyclic voltammetry (CV) tests of Li||Cu half batteries were conducted. Similarly, the MSP-IPL-coated Cu electrodes (denoted as MSP-IPL@Cu) for assembling Li||Cu half batteries were also prepared by the drop-casting method. Compared with the CV curves of bare Cu electrodes (Figure S17), the CV plot of MSP-IPL@Cu exhibited an additional signal peak at 1.21 V, corresponding to the lithiation of urea linkages (Figure 2a).[33] This indicated that the abundant urea linkages in the metallo-supramolecular polymer could serve as the uniformly distributed Li nucleation sites, improving the uniformity of Li deposition. To further verify the lithiation of urea linkages during the initial Li plating process, the paramagnetic center of lithiated Ti-PEA-IPDI and pristine Ti-PEA-IPDI was tested by electron paramagnetic resonance (EPR) spectroscopy. Compared with the EPR spectrum of pristine Ti-PEA-IPDI without signal response (Figure 2b), a significant EPR signal was detected for the lithiated Ti-PEA-IPDI, which was mainly attributed to the decreased charge screening resulting from the presence of Li ions.[34] The EPR result confirmed the formation of lithiated Ti-PEA-IPDI MSP-IPL, which could provide diffusion paths for Li^+ transportation, as well as slow down and homogenize the Li^+ flux near the Li metal surface.

To testify the superiority of MSP-IPL in boosting Li plating/stripping reversibility, the electrochemical performances of Li||Cu half batteries were measured based on MSP-IPL@Cu and bare Cu electrodes. As shown in Figure 2c, the average CE of the batteries with MSP-IPL@Cu was up to 98.8% during 50 Li plating/stripping cycles. In comparison, the batteries with bare Cu only delivered an average CE of 84.4%. The initial Li plating profiles of Li||Cu half batteries were further analyzed to investigate the effect of MSP-IPL on mass-transfer and nucleation overpotentials (Figure 2d). When using the MSP-IPL@Cu as current collectors, the mass-transfer and nucleation overpotentials of batteries were 26.4 and 72.3 mV, respectively (Figure S18), both of which were lower than those of batteries with bare Cu (41.2 and 136.0 mV), revealing that the MSP-IPL could efficiently improve the mass-transfer kinetics of electrodes and significantly reduce the energy barrier of Li nucleation. The prolonged Li plating/stripping cycling of Li||Cu half batteries was also investigated to check long-term reversibility of the MSP-IPL@Cu (Figure 2e). At 1.0 mA cm^{-2} with a capacity of 2.0 mAh cm^{-2}, the batteries with MSP-IPL@Cu displayed impressive Li plating/stripping stability for over 420 cycles, delivering a well-maintained CE of 98.11%. In contrast, apparent CE fluctuation was observed for the batteries with bare Cu after less than 100 cycles, indicating battery failure. Significant differences of MSP-IPL@Cu and bare Cu in Li plating/stripping reversibility were partially ascribed to the key role of MSP-IPL in accelerating Li^+ transfer, which was also verified by electrochemical impedance spectroscopy (EIS) and CV measurements. Compared with the batteries assembled with bare Cu (Figure S19), the batteries with MSP-IPL@Cu exhibited much lower interfacial resistances before and after cycling. Moreover, the CV curves for MSP-IPL@Cu

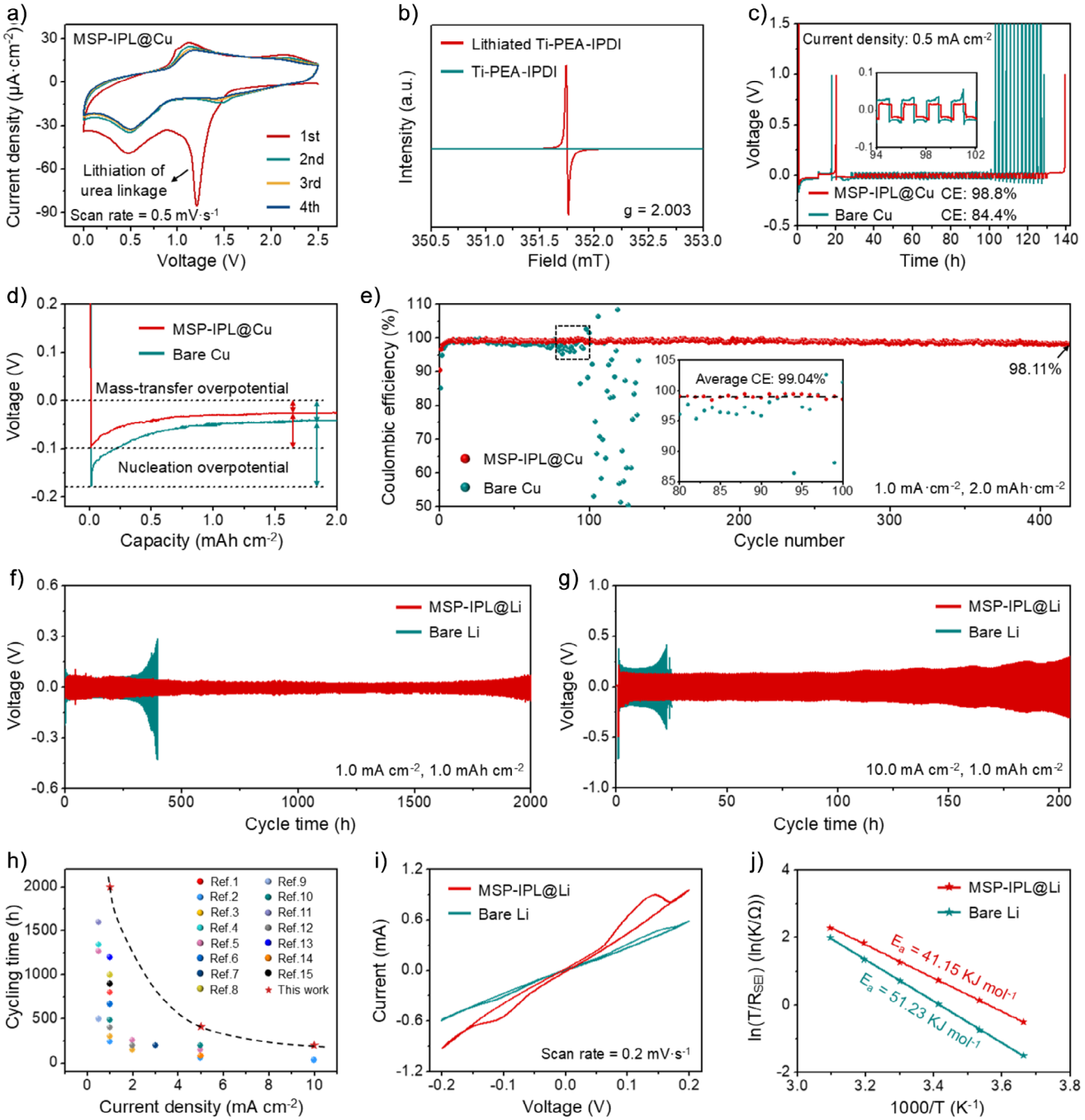

Figure 2. Electrochemical performances of Li||Cu half batteries assembled with MSP-IPL@Cu and bare Cu and Li||Li symmetric batteries assembled with MSP-IPL@Li and bare Li. a) CV curves of Li||Cu half batteries assembled with MSP-IPL@Cu at a scan rate of 0.5 mV s^{-1} from 0 to 2.5 V. b) EPR spectra of lithiated Ti-PEA-IPDI and pristine Ti-PEA-IPDI metallo-supramolecular polymers. c) Voltage–time curves of the Li||Cu half batteries at 0.5 mA cm^{-2} for calculating the average CEs. d) Initial Li plating profiles of Li||Cu batteries measured at 0.5 mA cm^{-2}. e) CE test for long-term cycling of Li||Cu half batteries at 1.0 mA cm^{-2} with a capacity of 2.0 mAh cm^{-2}. Inset: enlarged view of CE test for Li||Cu half batteries at 80–100 cycles. Galvanostatic cycling stability of Li||Li symmetric batteries measured at f) 1.0 mA cm^{-2} with a capacity of 1.0 mAh cm^{-2} and g) 10.0 mA cm^{-2} with a capacity of 1.0 mAh cm^{-2}. h) Comparison of the cycle lifespan for Li||Li symmetric batteries based on MSP-IPL@Li and those of previously reported Li electrodes stabilized by various artificial SEI layers. i) CV curves of Li||Li symmetric batteries measured at a scan rate of 0.2 mV s^{-1} from −0.2 to 0.2 V. j) Arrhenius behavior of the reciprocal R_{SEI} and the calculated E_a for Li^+ diffusion through SEI on the MSP-IPL@Li and bare Li.

exhibited higher current responses than bare Cu (Figure S20), illustrating the achievement of rapid Li^+ transport and accelerated reaction kinetics.

To evaluate the reliability of Ti-PEA-IPDI MSP-IPL and its compatibility with LMAs, the cycling stability of Li||Li symmetric batteries was further investigated. When cycled at 1.0 mA cm^{-2} with a capacity of 1.0 mAh cm^{-2} (Figure 2f), the batteries with MSP-IPL@Li displayed outstanding cycling stability for over 2000 h with an ultralow overpotential of ~71 mV, demonstrating improved interfacial stability and smooth mass-transfer process. In sharp contrast, the batteries with bare Li could only work stably for less than 300 h, and then showed the sharply increased voltage hysteresis exceeding 370 mV, indicating that the batteries suffered from uncontrollable Li dendrite proliferation and excessive electrolyte consumption. When the current density increased to 5.0 mA cm^{-2}, the batteries with bare Li exhibited a sharp voltage divergence to ~273 mV after merely 58 h and failed quickly after 65 h (Figure S21a). However, the batteries with MSP-IPL@Li showed steady Li plating/stripping behaviors for over 413 h and low voltage hysteresis of ~120 mV. At a higher current density of 10.0 mA cm^{-2}, the batteries with bare Li encountered continuous increase in voltage hysteresis, reaching 418 mV after cycling for only 22 h (Figure 2g), whereas the batteries with MSP-IPL@Li could stably cycle for over 205 h with limited voltage polarization. The cycling performance of Li||Li symmetric batteries at high capacities was also concerned. For the batteries with bare Li, a severe short circuit was occurred after merely 39 h at 5.0 mA cm^{-2} with a capacity of 5.0 mAh cm^{-2} (Figure S21b). By comparison, the batteries with MSP-IPL@Li could still maintain a stable cycling process for more than 203 h, fully confirming the crucial role of MSP-IPL in stabilizing LMAs. Impressively, the extraordinary cycling stability of MSP-IPL@Li is highly competitive compared to most of reported LMAs modified by interface engineering (Figure 2h and Table S2).[12,13,15–17,35–44] Furthermore, the rate performance of Li||Li symmetric batteries was also tested at various current densities from 1.0 to 20.0 mA cm^{-2} (Figure S22). For the batteries with bare Li, the voltage hysteresis sharply increased from 75 to 360 mV with the increase of current densities from 1.0 to 10.0 mA cm^{-2}. As the current densities further increased, the irregular voltage–time curves of batteries were observed, indicating that stable Li plating/stripping is difficult for bare Li at such high current densities. In contrast, the batteries with MSP-IPL@Li exhibited flat and regular voltage platforms even at 20.0 mA cm^{-2}. The significantly decreased overpotentials were around 16, 50, 82, 105, and 122 mV at the current densities of 1.0, 5.0, 10.0, 15.0, and 20.0 mA cm^{-2}, respectively.

The thickness of MSP-IPL, as a key indicator determining its physicochemical properties, significantly affects its protective effect on LMAs. In view of this, we controlled the thickness of MSP-IPL by adding different amounts of precursor solution dropwise on the Li metal surface and studied the effect of the thickness of MSP-IPL on Li plating/stripping stability based on Li||Li symmetric batteries. As shown in Figure S23, the MSP-IPL@Li electrodes prepared by adding 50 μL precursor solution dropwise (corresponding to the thickness of 1.6 μm) exhibited the best cycling stability compared with the others. The results of EIS analyses based on Li||Li symmetric batteries also indicated that the MSP-IPL@Li electrodes prepared by adding 50 μL precursor solution dropwise could achieve the lowest interfacial resistance (Figure S24). Above results fully demonstrated the necessity of thickness control, which was conducive to achieving coordination and balance of the comprehensive performances of MSP-IPL, and ensuring the maximum protection effect of MSP-IPL. Therefore, the MSP-IPL@Li electrodes covered by a 1.6 μm thick MSP-IPL were adopted for all electrochemical measurements and characterizations in this work.

The significantly accelerated charge transfer kinetics of MSP-IPL@Li was further verified through a series of electrochemical kinetic measurements. The CV curves of Li||Li symmetric batteries were tested at the voltage range from −0.2 to 0.2 V. As displayed in Figure 2i, the typical centrosymmetric loops reflected the reversible electrochemical behavior for these two electrodes. Compared with the bare Li, the MSP-IPL@Li demonstrated a more pronounced current response, indicating higher Li plating/stripping reversibility and faster Li^+ transfer for the MSP-IPL@Li.[45] Exchange current densities (i_0) were also calculated based on the Tafel plots of Li||Li symmetric batteries (Figure S25). The i_0 value of MSP-IPL@Li was as high as 1.045 mA cm^{-2}, much higher than that of bare Li (0.294 mA cm^{-2}), indicating that the MSP-IPL@Li/electrolyte interface supported faster ion transport. Furthermore, apparent activation energies (E_a) for Li^+ diffusion through the SEI were calculated by linearly fitting $\ln(T/R_{SEI})$ versus $1/T$ (Figure S26). For the MSP-IPL@Li, the E_a value was only 41.15 kJ mol^{-1} (Figure 2j), whereas it was up to 51.23 kJ mol^{-1} when using the bare Li, fully confirming the favorable mass-transfer kinetics of the constructed MSP-IPL.[46] To more intuitively quantify the ion-transfer ability of the constructed MSP-IPL, we measured and calculated the ionic conductivity of the electrolyte-wetted Ti-PEA-IPDI layer (Figures S27–S29). According to the calculation results, the ionic conductivity of the electrolyte-wetted Ti-PEA-IPDI layer, specifically the apparent ionic conductivity of Ti-PEA-IPDI layer, reached a considerable value of 0.485 mS cm^{-1} at room temperature. This value was very competitive even compared with many polymer electrolytes containing a large amount of Li salts, thus fully validating the superior Li^+ transport capability of Ti-PEA-IPDI as the interfacial protective layer. We further measured the apparent ionic conductivity of the Ti-PEA-IPDI layer at different temperatures and calculated the activation energy (E_a) of Li^+ transport by fitting the linear relationship between the common logarithm of ionic conductivities and the temperatures. The electrolyte-wetted Ti-PEA-IPDI layer displayed a low E_a of 0.337 eV, fully verifying the rationality of molecular structure design for Ti-PEA-IPDI and the high-efficient Li^+ transport achieved by MSP-IPL.

To directly verify the effectiveness of the constructed MSP-IPL in suppressing Li dendrite growth, the surface morphology of MSP-IPL@Li and bare Li after different cycles was systematically investigated by SEM technique. For the bare Li, a coarse and porous surface morphology was

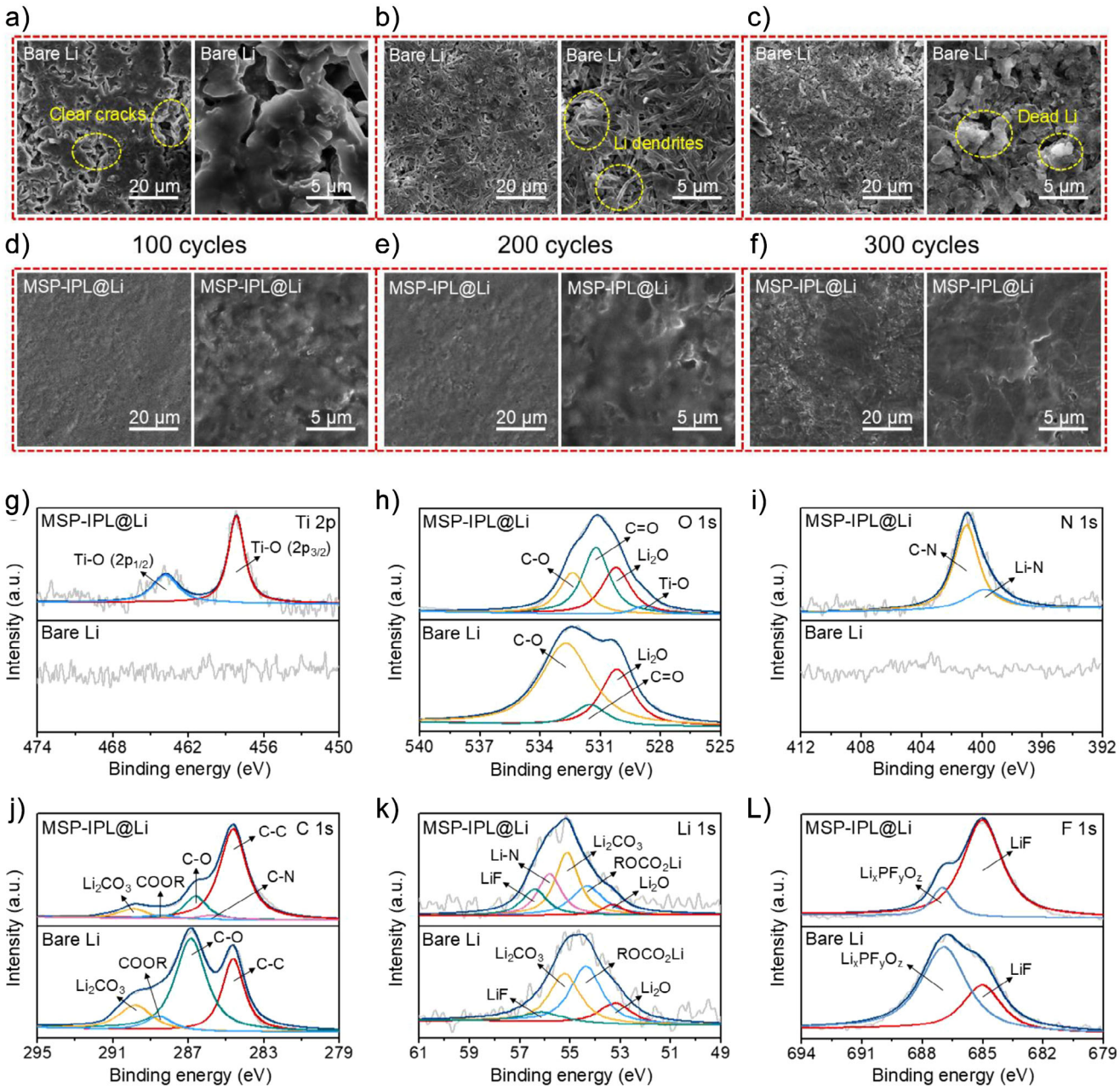

Figure 3. Surface morphology and composition characterizations of the cycled MSP-IPL@Li and bare Li. Top-view SEM images of bare Li retrieved from Li||Li symmetric batteries after a) 100, b) 200, and c) 300 cycles. Top-view SEM images of MSP-IPL@Li retrieved from Li||Li symmetric batteries after d) 100, e) 200, and f) 300 cycles. High-resolution XPS spectra at g) Ti 2p, h) O 1s, i) N 1s, j) C 1s, k) Li 1s, and l) F 1s regions of MSP-IPL@Li and bare Li retrieved from Li||Li symmetric batteries after 20 cycles.

observed clearly after only 100 cycles (Figure 3a). As the Li plating/stripping process continued for 200 cycles, the surface morphology of bare Li was further deteriorated (Figure 3b), presenting a loose surface completely covered by Li dendrites. When further increasing the Li plating/stripping process to 300 cycles, the bare Li exhibited a completely damaged surface morphology. Severely proliferated dead Li almost covered the entire surface of bare Li (Figure 3c). Evidently, the bare Li suffered from serious electrolyte corrosion, and the fragile native SEI could hardly provide protection for fresh Li metal. After constructing a protective MSP-IPL on the bare Li, significant improvement in surface morphology was detected. After 100 cycles, the MSP-IPL@Li presented a smooth and dense surface without any visible cracks (Figure 3d). When the MSP-IPL@Li was further cycled to 200 cycles, its flat and homogeneous surface could still be observed without the growth of Li dendrites (Figure 3e). Even after 300 cycles, the dense and dendrite-free surface morphology was still well maintained (Figure 3f), fully highlighting the key role of MSP-IPL in regulating Li electroplating behavior and inhibiting Li dendrite growth. The distinct differences in Li plating/stripping morphology were also demonstrated by

cross-section SEM characterization (Figure S30). In contrast to the rough and heavily pulverized surface of bare Li, the cycled MSP-IPL@Li electrodes exhibited a uniform and compact cross-section morphology, confirming the improvement effect of the MSP-IPL on Li plating uniformity. To more intuitively reveal the difference in surface morphology evolution of MSP-IPL@Li and bare Li, in situ optical microscopy observation was performed to monitor the Li plating/stripping process in real time. For the bare Li (Figure S31a), the original smooth and flat surface was covered by visible Li dendrites only after 100 cycles, presenting a rough and uneven surface morphology. As the Li plating/stripping process continued, the nonuniform Li deposition was further aggravated. Finally, the bare Li surface was fully covered by dendritic and dead Li after 300 cycles. In sharp contrast, steady Li plating/stripping behaviors was achieved when using the MSP-IPL@Li (Figure S31b). Throughout the entire cycle, the smooth and dense electrode surface was well maintained without any visible Li dendrites, fully demonstrating that the constructed MSP-IPL could efficiently facilitate uniform Li deposition and enhance interfacial stability.

The difference in surface chemical composition of the cycled MSP-IPL@Li and bare Li was identified by EDX and X-ray photoelectron spectroscopy (XPS) analysis. As displayed in Figure S32, EDX spectrum and corresponding elemental mappings of the cycled MSP-IPL@Li presented the uniform distribution of C, N, O, F, P, and Ti elements, illustrating the constructed MSP-IPL could tightly adhere to the Li electrodes and participate in the formation of SEI, which were greatly conducive to improving interfacial stability and promoting uniform Li deposition. The surface composition evolution was further characterized in detail by XPS technique. The Ti 2p spectrum of MSP-IPL@Li exhibited a pair of distinct signal peaks of Ti—O species (Figure 3g), which are consistent with the peak position of Ti—O species detected on the fresh MSP-IPL@Li. This indicated Ti-PEA-IPDI metallo-supramolecular polymer was not only involved in the formation of SEI but also its molecular structure remained stable during the repeated cycling process. The result of O 1s spectra also supported the above conclusion. In addition to C—O, C═O, and Li_2O signal peaks, an extra characteristic peak was detected at 528.8 eV in the O 1s spectrum of MSP-IPL@Li, corresponding to Ti—O species (Figure 3h). The notable differences in surface composition were highlighted by the N 1s spectra. Compared with the bare Li surface with an absence of nitrogenous species, the N 1s spectrum of MSP-IPL@Li displayed two characteristic peaks at 401.0 and 399.8 eV (Figure 3i), corresponding to C—N and Li—N, respectively, which further confirmed the formation of MSP-IPL-derived SEI and the lithiation of urea linkages. For the C 1s spectra, four typical peaks assigned to Li_2CO_3, COOR, C—O, and Li_2O species were detected on both MSP-IPL@Li and bare Li surfaces (Figure 3j). However, it was noteworthy that the peak areas of COOR and C—O species for the bare Li were obviously larger than those for the MSP-IPL@Li, illustrating that the native SEI formed on the bare Li could hardly provide efficient protection for metallic Li to prevent electrolyte corrosion. Regarding the Li 1s spectra, a significant characteristic signal of Li—N species was identified on the MSP-IPL@Li surface (Figure 3k), which was consistent with the result of N 1s spectra. Moreover, a larger peak area of LiF species was observed for the MSP-IPL@Li, illustrating a higher LiF content in the MSP-IPL-derived SEI, which was further verified by F 1s spectra. As shown in Figure 3l, higher LiF content and lower $Li_xPF_yO_z$ content were detected on the MSP-IPL@Li surface. This is mainly because the uniformly distributed Ti-POMs in polymer skeleton can effectively bind with PF_6^- anions in electrolytes, thereby promoting PF_6^- decomposition, which will be elaborated in detail in the subsequent discussion. To further verify the involvement of MSP-IPL in SEI formation, we also conducted in-depth XPS analysis for the cycled MSP-IPL@Li electrode after Ar^+ sputtering for 5 min. The test results demonstrated that the MSP-IPL-derived SEI exhibited no obvious differences in chemical compositions and relative contents of constituent species between its surface and bulk regions (Figure S33). Therefore, it was confirmed that the constructed MSP-IPL participated in the formation of SEI, and the MSP-IPL-derived SEI possessed uniform compositions and high chemical stability, ensuring the sustained protection for Li metal anodes during long-term cycling.

To demonstrate the feasibility and practicality of MSP-IPL@Li, the high-loading Li||LFP and Li||NCM811 batteries were assembled and systematically tested. When assembled with the bare Li anodes, the high-loading Li||LFP batteries exhibited a significant capacity decay at 1.0 C (Figure 4a). After 200 cycles, the specific discharge capacity of batteries was only 21.4 mAh g^{-1}, indicating that the instability of the bare Li/electrolyte interface severely exacerbated the side reactions and the batteries were close to failure. When using the MSP-IPL@Li as anodes, the high-loading Li||LFP batteries achieved extraordinary improvement in cycling stability, presenting a significantly prolonged cycling lifespan for over 600 cycles with a considerable remaining capacity of 132.8 mAh g^{-1} corresponding to a capacity retention of 86.2%. The rate performance of high-loading Li||LFP batteries was also studied using different anodes (Figure 4b). For the batteries assembled with bare Li anodes, the reversible discharge capacity was up to 147.3 mAh g^{-1} at 1.0 C, but sharply dropped to only 44.0 mAh g^{-1} at 5.0 C, which was mainly due to the poor mass-transfer kinetics at the bare Li/electrolyte interface. By comparison, the batteries assembled with MSP-IPL@Li exhibited well-maintained reversible discharge capacities of 153.8, 139.5, 131.4, 123.4, and 114.8 mAh g^{-1} at the current densities of 1.0, 2.0, 3.0, 4.0, and 5.0 C, respectively, highlighting the superiorities of MSP-IPL@Li anodes in fast charge–discharge. The outstanding rate performance of MSP-IPL@Li anodes should be ascribed to the lower polarization and better reaction kinetics than bare Li anodes, which were confirmed by the smaller potential differences between charge–discharge plateaus at various current rates of MSP-IPL@Li anodes (Figure 4c,d).

As a high-capacity layered cathode material, Ni-rich NCM811 is deemed as one of the most promising candidates for the construction of high-specific-energy Li metal batteries.

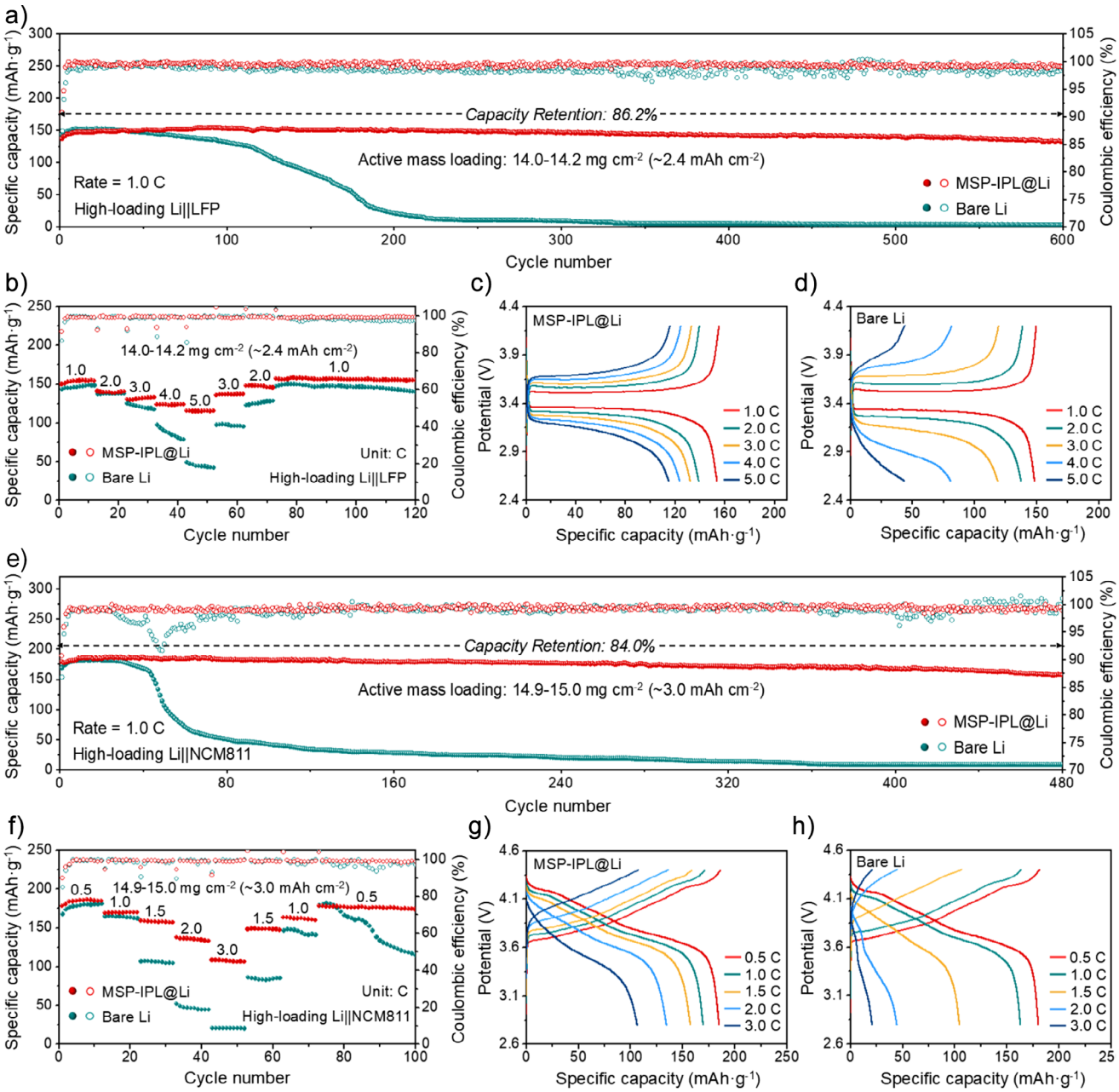

Figure 4. Electrochemical performances of high-loading Li||LFP and Li||NCM811 batteries assembled with MSP-IPL@Li and bare Li anodes. a) Cycling performance of high-loading Li||LFP batteries measured at 1.0 C (1.0 C = 170 mA g^{-1}). b) Rate performance of high-loading Li||LFP batteries measured at various current rates from 1.0 to 5.0 C. Galvanostatic charge–discharge profiles of high-loading Li||LFP batteries assembled with c) MSP-IPL@Li and d) bare Li anodes at various current rates from 1.0 to 5.0 C. e) Cycling performance of high-loading Li||NCM811 batteries measured at 2.8–4.4 V and 1.0 C (1.0 C = 200 mA g^{-1}). f) Rate performance of high-loading Li||NCM811 batteries measured at various current rates from 0.5 to 3.0 C. Galvanostatic charge–discharge profiles of high-loading Li||NCM811 batteries assembled with g) MSP-IPL@Li and h) bare Li anodes at various current rates from 0.5 to 3.0 C.

In view of this, we assembled and tested high-loading Li||NCM811 batteries to further verify the practical potential of MSP-IPL@Li anodes. When cycled at 1.0 C (Figure 4e), the batteries assembled with bare Li anodes suffered from severe capacity degradation and remarkable CE fluctuations after only 40 cycles, and the specific discharge capacity of the batteries rapidly decayed to 51 mAh g^{-1} after 80 cycles. When the MSP-IPL@Li anodes were paired with NCM811 cathodes, the batteries exhibited markedly improved cycling stability, delivering a high remaining capacity of 156.9 mAh g^{-1} after 480 cycles, corresponding to a capacity retention of 84.0%. Notably, the capacity increase phenomenon was observed for both MSP-IPL@Li||LFP and MSP-IPL@Li||NCM811 batteries during the initial cycles, which was mainly due to the lithiation of urea linkages on the anodic side and the optimization of Li^+ insertion/extraction pathways on the cathodic

side during the initial Li plating process. Furthermore, the rate performance of high-loading Li||NCM811 batteries was also tested at stepwise current densities from 0.5 to 3.0 C (Figure 4f). For the batteries assembled with bare Li anodes, the specific discharge capacities decreased markedly with the increase of current rates. Especially at 3.0 C, the batteries only delivered a reversible discharge capacity of 20.7 mAh g^{-1}, indicating the sluggish reaction kinetics of bare Li anodes. In contrast, the batteries assembled with MSP-IPL@Li anodes exhibited significantly increased capacity retention, delivering high reversible capacities of 184.4, 169.3, 158.3, 135.3, and 107.8 mAh g^{-1} at 0.5, 1.0, 1.5, 2.0, and 3.0 C, respectively. By further examining the charge–discharge voltage curves of batteries, it was found that the batteries assembled with MSP-IPL@Li anodes exhibited much lower voltage polarization especially at high current rates (Figure 4g,h), further verifying the improved interfacial stability and mass-transfer kinetics of MSP-IPL@Li anodes.

Encouraged by the enhanced electrochemical performance of excess Li||NCM811 batteries, we further assembled Li||NCM811 batteries with a low N/P ratio of ~2.86 by pairing 50-µm-thick MSP-IPL@Li or bare Li anodes (~10 mAh cm^{-2}) with high-loading NCM811 cathodes (~3.5 mAh cm^{-2}) and tested their cycling performances under practical conditions. As shown in Figure S34, the Li||NCM811 batteries with 50-µm-thick MSP-IPL@Li anodes exhibited exceptional cycling performance with a considerable capacity retention of 90.3% after 80 cycles, much higher than that of Li||NCM811 batteries with 50-µm-thick bare Li anodes. Raising the charging cut-off voltage is considered one of the effective strategies to enhance the energy density of Li metal batteries. However, achieving stable operation of Li metal batteries at high voltages poses severe challenges for the stability of both LMAs and cathodes. To verify the compatibility of MSP-IPL@Li anodes with high-voltage cathodes, practical Li||NCM811 batteries were further tested under a high operating voltage of 4.7 V (versus Li/Li^+). After activation for 2 cycles at a low current rate of 0.2 C, the batteries assembled with bare Li anodes displayed continuous capacity fading at 0.5 C (Figure S35). After 65 cycles, the specific discharge capacity of batteries was only 38.1 mAh g^{-1}. However, when assembled with the MSP-IPL@Li anodes, the batteries demonstrated impressive cycling stability, delivering a considerable remaining capacity of 158.3 mAh g^{-1} after 260 cycles. Further investigation of galvanostatic voltage profiles confirmed that the 4.7 V-class MSP-IPL@Li||NCM811 batteries achieved lower voltage hysteresis and more stable charge–discharge process (Figure S36), illustrating the significantly boosted reaction kinetics and interfacial stability of MSP-IPL@Li anodes.

To gain insight into the reasons for the distinguished electrochemical performance of batteries assembled with MSP-IPL@Li, the working mechanism of Ti-PEA-IPDI MSP-IPL was revealed by combining theoretical calculations and experimental investigations. The COMSOL Multiphysics simulation for the MSP-IPL@Li and bare Li anodes was conducted to probe the surface morphology evolution and local current density distribution (Figure 5a). For the bare Li, the original protrusions on the bare Li surface inevitably resulted in uneven distribution of electric field at the electrode–electrolyte interface and initial nonuniform Li nucleation. As the Li plating process continued, the nonuniformity of local current density distribution was further exacerbated, and the bare Li presented a severely deteriorated surface morphology. When the bare Li was covered with the MSP-IPL, the elimination of the original protrusions greatly evened out the electric field at the electrode–electrolyte. Moreover, due to the abundant urea linkages in the Ti-PEA-IPDI served as the uniformly distributed Li nucleation sites, a more uniform local current density distribution and a flatter surface morphology were achieved for the MSP-IPL@Li as the Li plating process continued (Figure 5b). Density functional theory (DFT) calculations were performed systematically to deeply investigate the effect of Ti-POMs in polymer skeleton on electrolyte solvation chemistry. Electrostatic potential (ESP) calculation of Ti_6(HPAB) demonstrated the electron deficiency of Ti atoms due to the electron-withdrawing property of coordinating O atoms (Figures S37 and 5c). Charge distribution of Ti_6(HPAB) based on Mulliken populations further quantitatively proved the electropositivity of Ti atoms (Figure 5d), implying a possible interaction between the Ti-POMs in polymer skeleton with PF_6^- anions in electrolytes. To verify this inference, the geometries of Ti_6(HPAB)-PF_6^- was optimized and the binding energy between Ti_6(HPAB) and PF_6^- was calculated. As a result, a binding energy of −0.993 eV existed between Ti_6(HPAB) and PF_6^- (Figure 5e and Table S3), illustrating that the construction of MSP-IPL was expected to limit PF_6^- migration and promote Li^+ transfer, thus achieving improved Li^+ concentration gradient.

The results of spectral characterization further verified the above conclusion. Fourier transform infrared (FTIR) spectra of pristine $LiPF_6$ powder, NMP solutions of $LiPF_6$, and Ti-PEA-IPDI/$LiPF_6$ (denoted as $LiPF_6$-NMP and Ti-PEA-IPDI/$LiPF_6$-NMP) were tested (Figure 5f). It should be noted that the reason for choosing NMP as the solvent instead of carbonate-based electrolyte (CBE) for FTIR characterizations is that the prepared Ti-PEA-IPDI is almost insoluble in the CBE (Figure S38). Compared with the typical absorption peak of unsolvated PF_6^- for the pristine $LiPF_6$, a remarkable blueshift (10.2 cm^{-1}) was detected in the $LiPF_6$-NMP, confirming the participation of PF_6^- in Li^+ solvation sheath.[47] When introducing the Ti-PEA-IPDI into $LiPF_6$-NMP, a detectable redshift (7.3 cm^{-1}) was observed compared with the absorption peak of solvated PF_6^- for the $LiPF_6$-NMP, illustrating that PF_6^- anions were partly removed from the Li^+ solvation sheath due to the binding of Ti-POMs on PF_6^- anions. To further probe the transition of electrolyte solvation structure, nuclear magnetic resonance (NMR) technology was conducted based on $LiPF_6$-NMP and Ti-PEA-IPDI/$LiPF_6$-NMP in dimethyl sulfoxide-d_6 (DMSO-d_6) solutions (denoted as $LiPF_6$-NMP/DMSO and Ti-PEA-IPDI/$LiPF_6$-NMP/DMSO). When introducing the Ti-PEA-IPDI into $LiPF_6$-NMP/DMSO, the ^7Li signal peak shifted from −0.63 to −0.58 ppm (Figure 5g), demonstrating a deshielding effect caused by the removal of PF_6^- anions,[48] which was also supported by the chemical shift in ^{19}F spectra. After the addition of Ti-PEA-IPDI, the ^{19}F signals assigned to PF_6^- showed significant downfield shifts (Figure 5h), indicating the weakened interaction of Li^+ and PF_6^-.[49]

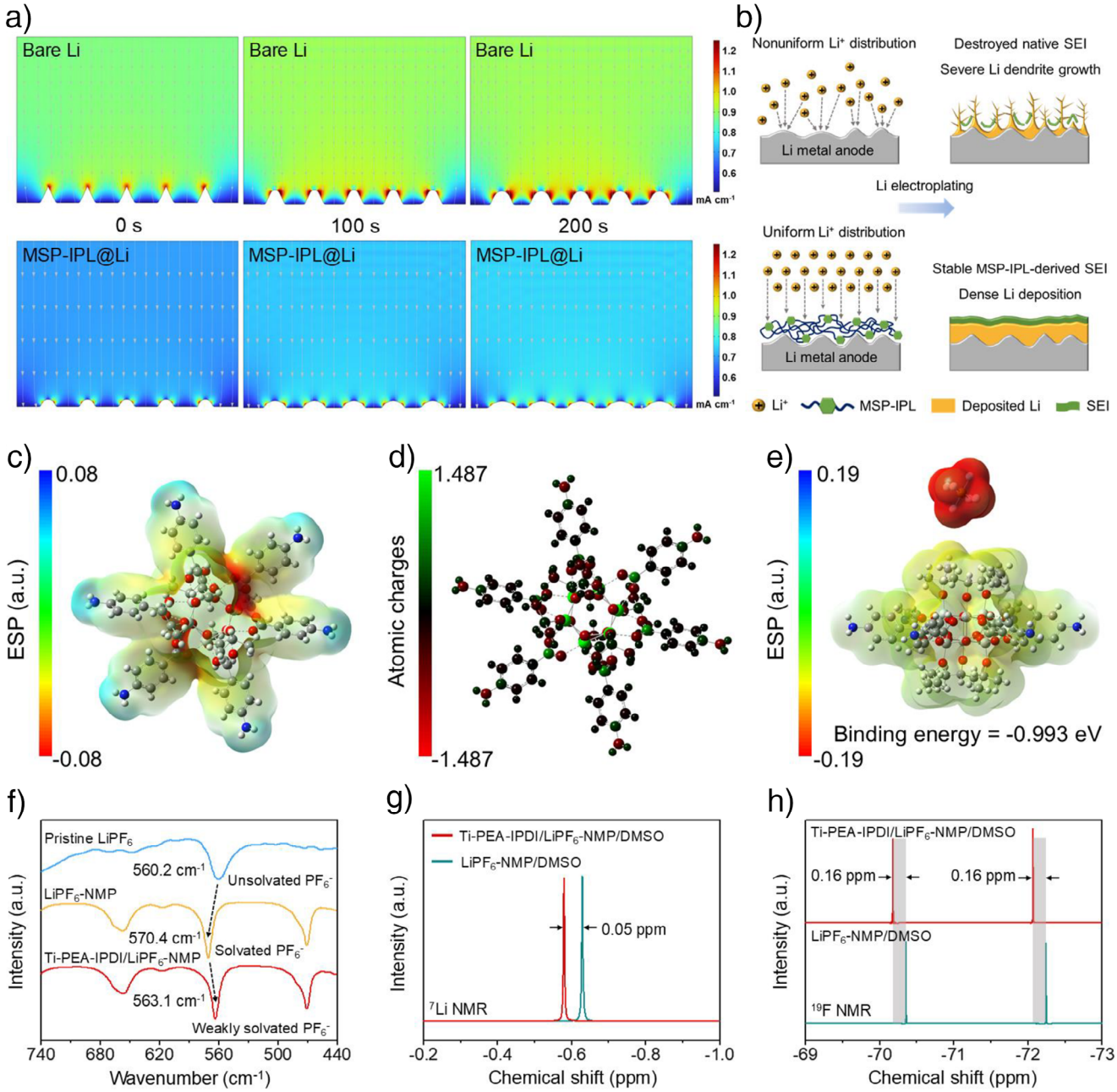

Figure 5. Working mechanism of Ti-PEA-IPDI metallo-supramolecular polymer as an artificial interfacial layer. a) COMSOL Multiphysics simulation of local current density distribution and surface morphology evolution for bare Li (upper) and MSP-IPL@Li (lower). b) Schematic illustration of the Li deposition behaviors based on bare Li (upper) and MSP-IPL@Li (lower). c) Electrostatic potential (ESP) mapping of Ti_6(HPAB). d) Charge distribution of Ti_6(HPAB) based on Mulliken populations. e) Binding energy calculation between Ti_6(HPAB) and PF_6^-. f) FTIR spectra of pristine $LiPF_6$, $LiPF_6$-NMP, and Ti-PEA-IPDI/$LiPF_6$-NMP. g) ^{7}Li NMR spectra and h) ^{19}F NMR spectra of Ti-PEA-IPDI/$LiPF_6$-NMP/DMSO and $LiPF_6$-NMP/DMSO.

Molecular dynamics (MD) simulations were performed to further clarify the changes of Li^+ solvation structure (Figure S39). According to the results of radial distribution functions (RDFs), the Li^+-P(PF_6^-) peak at the distance of 2.08 exhibited a lower intensity after introducing Ti_6(HPAB) into $LiPF_6$-NMP (denoted as Ti_6(HPAB)/$LiPF_6$-NMP). The coordination number of Li^+-P(PF_6^-) also decreased from 1.323 of $LiPF_6$-NMP to 1.083 of Ti_6(HPAB)/$LiPF_6$-NMP, confirming the partial removal of PF_6^- anions due to the limiting effect of Ti-POMs. These simulation results agreed with the FTIR and NMR characterization results, fully verifying the reliability of the experimental conclusion. Apparently, both theoretical and experimental results demonstrated that the uniformly distributed Ti-POMs in polymer skeleton could effectively bind with PF_6^- anions in electrolytes via electrostatic interactions, promoting Li^+ fast migration and homogenizing Li^+ concentration gradient near the electrode–electrolyte interfaces.

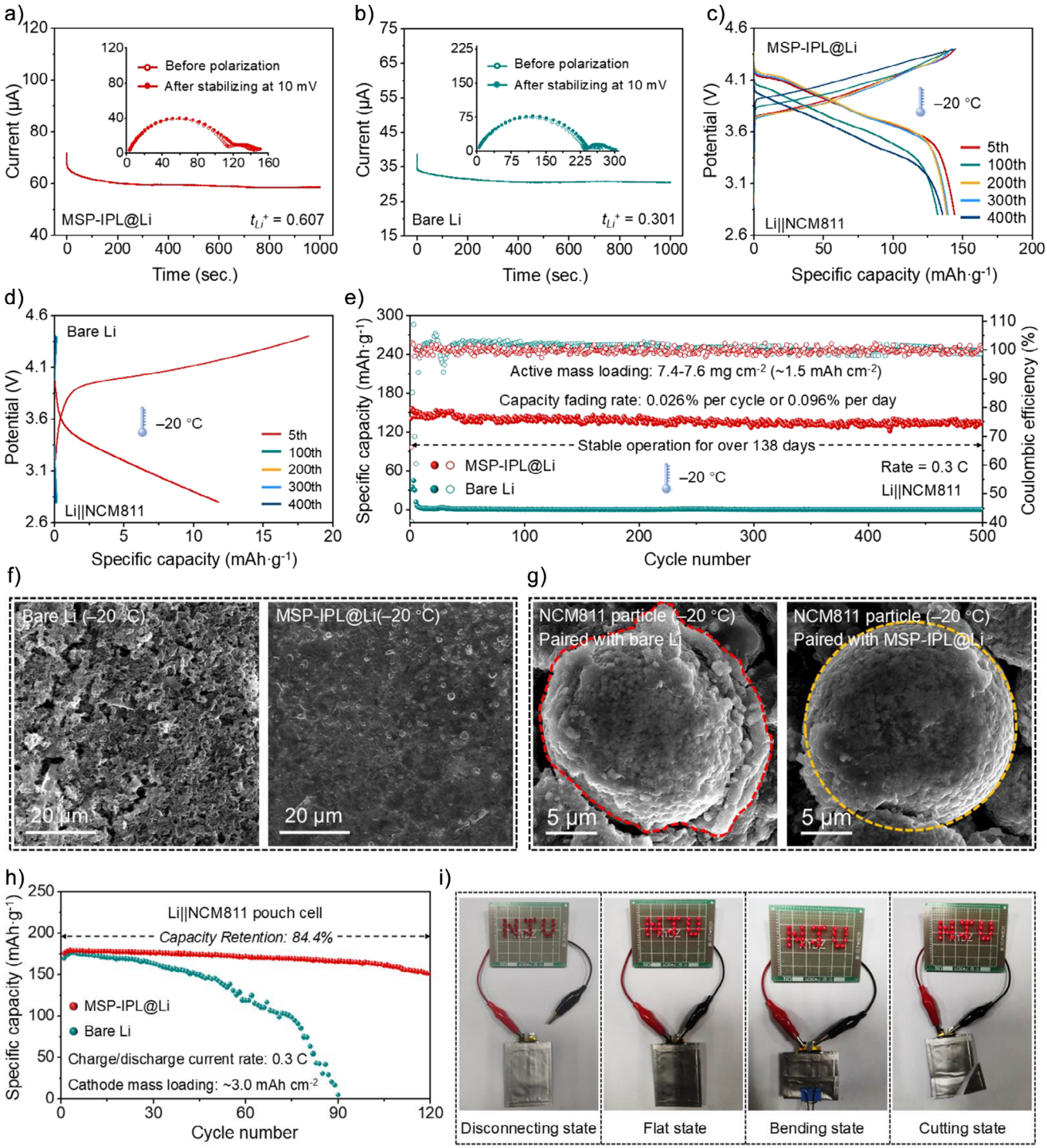

Figure 6. Low-temperature performances of Li||NCM811 batteries assembled with MSP-IPL@Li and bare Li and practical evaluation of Li||NCM811 pouch batteries. Nyquist and chronoamperometry plots of Li||Li symmetric batteries assembled with a) MSP-IPL@Li and b) bare Li for the measurement of t_{Li}^+. Galvanostatic charge–discharge profiles of different cycles for Li||NCM811 batteries assembled with c) MSP-IPL@Li and d) bare Li anodes measured at −20 °C. e) Long-term cycling stability of Li||NCM811 batteries measured at a low temperature of −20 °C and 0.3 C. f) SEM investigation for the MSP-IPL@Li and bare Li anodes retrieved from Li||NCM811 batteries after 500 cycles at −20 °C. g) SEM investigation for the NCM811 cathodes retrieved from Li||NCM811 batteries after 500 cycles at −20 °C. h) Cycling performance of Li||NCM811 pouch batteries assembled with MSP-IPL@Li and bare Li anodes. i) Digital photos of the Li||NCM811 pouch batteries assembled with MSP-IPL@Li anodes continuously illuminating red LEDs at flat, bending, and cutting states.

To directly verify the above theoretical and experimental results, the t_{Li}^+ in the CBE paired with MSP-IPL@Li and bare Li electrodes was measured by monitoring the AC impedance of Li||Li symmetric batteries before and after DC polarization (Figure 6a,b). A significantly increased t_{Li}^+ was achieved in the CBE paired with MSP-IPL@Li (0.607), much higher than that in the CBE paired with bare Li (0.301), demonstrating the key role of MSP-IPL in increasing Li^+ flux and reducing concentration polarization near the electrode–electrolyte interfaces.[50] In consideration of improved Li^+ concentration gradient near the MSP-IPL@Li and high ion-transfer ability of MSP-IPL, the low-temperature cycling performance of Li||NCM811 batteries assembled with the MSP-IPL@Li and bare Li anodes were investigated. When cycled at −20 °C, the Li||NCM811 batteries assembled with MSP-IPL@Li anodes exhibited regular and well-shaped charge–discharge profiles with low voltage polarization at different cycles (Figure 6c), whereas the galvanostatic charge–discharge profiles of the batteries with bare Li anodes demonstrated huge voltage hysteresis, poor cycling reversibility, and rapid capacity attenuation (Figure 6d). This indicated the constructed MSP-IPL played a crucial role in enhancing the low-temperature performances of batteries. Figure 6e showed the long-term cycling stability of Li||NCM811 batteries at a low temperature of −20 °C and a current rate of 0.3 C. For the batteries with bare Li anodes, the specific discharge capacity rapidly decayed to nearly 0% after several cycles, indicating the batteries with bare Li anodes hardly worked properly at such a low temperature. When assembled with MSP-IPL@Li anodes, the batteries exhibited markedly improved low-temperature cycling performance. After 500 cycles, the batteries could still deliver a considerable capacity retention of 84.4% with a high average CE of 98.75%, demonstrating its great potential for large-scale application in different regions and climates.

The SEM characterization of the anodes and cathodes cycled at −20 °C was performed to deeply understand the distinct differences in low-temperature cycling performance of Li||NCM811 batteries. For the bare Li anodes, a rough and loose surface covered by a large amount of dead Li was observed after 500 cycles (Figure 6f). In contrast, the MSP-IPL@Li anodes displayed a flat and dense surface without any visible cracks and dendrites, highlighting the advantages of MSP-IPL in promoting uniform Li^+ flux and rapid Li^+ transfer. Significant difference in surface morphology was also detected on the cathode side (Figure 6g). After 500 cycles at −20 °C, the NCM811 cathodes paired with bare Li anodes displayed an irregularly shaped particle morphology with severe pulverizations. When paired with the MSP-IPL@Li anodes, the integrity and smoothness of NCM811 particles were greatly improved, presenting dense particle morphology without any holes and cracks, which indicated the achievement of high-efficient Li^+ intercalation/deintercalation of NCM811 cathodes when paired with the MSP-IPL@Li anodes. The impressive electrochemical performance of Li||NCM811 coin batteries assembled with the MSP-IPL@Li anodes encouraged us to further explore the application prospect of MSP-IPL@Li anodes in Li||NCM811 pouch batteries. As shown in Figure 6h, the Li||NCM811 pouch batteries assembled with MSP-IPL@Li anodes exhibited significantly improved cycling stability at 0.3 C, achieving a considerable capacity retention of 84.4% after 120 cycles. By comparison, the Li||NCM811 pouch batteries assembled with bare Li anodes experienced successive capacity fading, followed by the battery failure after 90 cycles. Additionally, the practical Li||NCM811 pouch batteries assembled with MSP-IPL@Li anodes were used to power electronic devices to further demonstrate their practical application potential. As displayed in Figure 6i, the assembled pouch batteries successfully illuminated a light-emitting diode (LED) with a clear caption of "NJU", and the fully charged pouch batteries could stably power the LED without internal short circuits or combustion in bending and cutting states, fully proving the high safety of the Li||NCM811 pouch batteries assembled with MSP-IPL@Li anodes in practical operation.

Conclusion

In summary, a structurally novel metallo-supramolecular polymer was rationally designed and synthesized by utilizing a Ti-POM as a hexatopic linker to bridge organic and inorganic moieties. By a convenient drop-casting method, we successfully built an advanced Ti-PEA-IPDI MSP-IPL on the LMA surface to achieve outstanding mechanical and chemical stability, accelerated reaction kinetics, and dendrite-free Li deposition of MSP-IPL@Li anodes. Due to the high film formation uniformity and mechanical tenacity of MSP-IPL, the as-obtained MSP-IPL@Li anodes effectively avoided nucleation and growth of Li dendrites caused by the tip effect. Moreover, the uniformly distributed Ti-POMs in polymer skeleton were able to effectively limit PF_6^- migration by the electrostatic interaction, which significantly increased t_{Li}^+ (0.607) of electrolytes, promoted homogeneous Li^+ flux, and ensured smooth Li plating morphologies. Consequently, a stable Li plating/stripping process of MSP-IPL@Li electrodes for over 2000 h was achieved in the Li||Li symmetric batteries at 1.0 mA cm^{-2}. The high-loading Li||LFP and Li||NCM811 batteries assembled with MSP-IPL@Li anodes demonstrated markedly prolonged cycling lifespans, ultrahigh cycling reversibility, and outstanding rate capability. Even under a low temperature of −20 °C, the MSP-IPL@Li||NCM811 batteries still worked stably for over 500 cycles, corresponding to 138 days, with a capacity retention of 86.8%. Our findings provide new insights for designing an advanced metallo-supramolecular polymer interfacial protective layer towards stabilizing Li metal anodes, presenting a promising strategy for the development of safe and stable Li metal batteries.

Acknowledgements

The authors appreciate the financial support from the National Natural Science Foundation of China (22479074, 22475096, 22425106, and 22271139), the General Project of the Joint Fund of Equipment Pre-research and the Ministry of Education (8091B02052407), the Natural Science Foundation of Jiangsu Province (BK20240400 and BK20241236), the

Science and Technology Major Project of Jiangsu Province (BG2024013), the Scientific and Technological Achievements Transformation Special Fund of Jiangsu Province (BA2023037), the Academic Degree and Postgraduate Education Reform Project of Jiangsu Province (JGKT24_C001), the Key Core Technology Open Competition Project of Suzhou City (SYG2024122), the Open Research Fund of Suzhou Laboratory (SZLAB-1308–2024-TS005), the Gusu Leading Talent Program of Scientific and Technological Innovation and Entrepreneurship of Wujiang District in Suzhou City (ZXL2021273), and the Chenzhou National Sustainable Development Agenda Innovation Demonstration Zone Provincial Special Project (2023sfq11).

Conflict of Interests

The authors declare no conflict of interest.

Data Availability Statement

The data that support the findings of this study are available from the corresponding author upon reasonable request.

Keywords: Coordinatively cross-linking strategy · Interfacial protective layer · Lithium metal batteries · Metallo-supramolecular polymer · Titanium(IV)–polyoxometalates

[1] M. Li, J. Lu, Z. Chen, K. Amine, *Adv. Mater.* **2018**, *30*, 1800561.
[2] B. Liu, J.-G. Zhang, W. Xu, *Joule* **2018**, *2*, 833–845.
[3] X. Cheng, R. Zhang, C. Zhao, Q. Zhang, *Chem. Rev.* **2017**, *117*, 10403–10473.
[4] M. D. Tikekar, S. Choudhury, Z. Tu, L. A. Archer, *Nat. Energy* **2016**, *1*, 16114.
[5] G. Lu, J. Nai, D. Luan, X. Tao, X. W. D. Lou, *Sci. Adv.* **2023**, *9*, eadf1550.
[6] Y. Liu, X. Tao, Y. Wang, C. Jiang, C. Ma, O. Sheng, G. Lu, X. W. D. Lou, *Science* **2022**, *375*, 739–745.
[7] Y. Zhao, T. Zhou, L. P. H. Jeurgens, X. Kong, J. W. Choi, A. Coskun, *Chem* **2023**, *9*, 1–16.
[8] X. Zhang, Y. Yang, Z. Zhou, *Chem. Soc. Rev.* **2020**, *49*, 3040–3071.
[9] Y. Xia, P. Zhou, X. Kong, J. Tian, W. Zhang, S. Yan, W. Hou, H. Zhou, H. Dong, X. Chen, P. Wang, Z. Xu, L. Wan, B. Wang, K. Liu, *Nat. Energy* **2023**, *8*, 934–945.
[10] J. Zhao, L. Liao, F. Shi, T. Lei, G. Chen, A. Pei, J. Sun, K. Yan, G. Zhou, J. Xie, C. Liu, Y. Li, Z. Liang, Z. Bao, Y. Cui, *J. Am. Chem. Soc.* **2017**, *139*, 11550–11558.
[11] Z. Wang, Y. Wang, C. Wu, W. K. Pang, J. Mao, Z. Guo, *Chem. Sci.* **2021**, *12*, 8945–8966.
[12] T. Chen, F. Meng, Z. Zhang, J. Liang, Y. Hu, W. Kong, X. Zhang, Z. Jin, *Nano Energy* **2020**, *76*, 105068.
[13] T. Chen, W. Kong, P. Zhao, H. Lin, Y. Hu, R. Chen, W. Yan, Z. Jin, *Chem. Mater.* **2019**, *31*, 7565–7573.
[14] A. C. Kozen, C.-F. Lin, A. J. Pearse, M. X. Hao, L. Hu, A. Schroeder, S.-B. Lee, G. W. Rubloff, M. Noked, *ACS Nano* **2015**, *9*, 5884–5892.
[15] R. Pathak, K. Chen, A. Gurung, K. M. Reza, B. Bahrami, F. Wu, A. Chaudhary, N. Ghimire, B. Zhou, W.-H. Zhang, Y. Zhou, Q. Qiao, *Adv. Energy Mater.* **2019**, *9*, 1901486.
[16] J. Wu, Z. Rao, X. Liu, Y. Shen, C. Fang, L. Yuan, Z. Li, W. Zhang, X. Xie, Y. Huang, *Adv. Mater.* **2021**, *33*, 2007428.
[17] Y. Zhao, D. Wang, Y. Gao, T. Chen, Q. Huang, D. Wang, *Nano Energy* **2019**, *64*, 103893.
[18] N.-W. Li, Y. Shi, Y.-X. Yin, X.-X. Zeng, J.-Y. Li, C.-J. Li, L.-J. Wan, R. Wen, Y.-G. Guo, *Angew. Chem. Int. Ed.* **2018**, *57*, 1505–1509.
[19] Y. Feng, Y. Li, J. Lin, H. Wu, L. Zhu, X. Zhang, L. Zhang, C.-F. Sun, M. Wu, Y. Wang, *Nat. Commun.* **2023**, *14*, 3639.
[20] Z. Yu, Y. Cui, Z. Bao, *Cell Rep. Phys. Sci.* **2020**, *1*, 100119.
[21] R. Xu, X. Cheng, C. Yan, X. Zhang, Y. Xiao, C. Zhao, J. Huang, Q. Zhang, *Matter* **2019**, *1*, 317–344.
[22] X. Wan, T. Mu, G. Yin, *Nano-Micro Lett.* **2023**, *15*, 99.
[23] C.-H. Li, J.-L. Zuo, *Adv. Mater.* **2020**, *32*, 1903762.
[24] C.-H. Li, C. Wang, C. Keplinger, J.-L. Zuo, L. Jin, Y. Sun, P. Zheng, Y. Cao, F. Lissel, C. Linder, X.-Z. You, Z. Bao, *Nat. Chem.* **2016**, *8*, 618–624.
[25] J.-C. Lai, X.-Y. Jia, D.-P. Wang, Y.-B. Deng, P. Zheng, C.-H. Li, J.-L. Zuo, Z. Bao, *Nat. Commun.* **2019**, *10*, 1164.
[26] R. D. Mukhopadhyay, A. Ajayaghosh, *Chem. Soc. Rev.* **2023**, *52*, 8635–8650.
[27] J. Xiang, C.-L. Ho, W.-Y. Wong, *Polym. Chem.* **2015**, *6*, 6905–6930.
[28] Y. K. Jeong, J. W. Choi, *ACS Nano* **2019**, *13*, 8364–8373.
[29] P. Zhai, L. Liu, X. Gu, T. Wang, Y. Gong, *Adv. Energy Mater.* **2020**, *10*, 2001257.
[30] Q. Zhao, S. Stalin, L. A. Archer, *Joule* **2021**, *5*, 1119–1142.
[31] Q.-K. Zhang, X.-Q. Zhang, J. Wan, N. Yao, T.-L. Song, J. Xie, L.-P. Hou, M.-Y. Zhou, X. Chen, B.-Q. Li, R. Wen, H.-J. Peng, Q. Zhang, J.-Q. Huang, *Nat. Energy* **2023**, *8*, 725–735.
[32] J. Huang, R. Meng, L. Zu, Z. Wang, N. Feng, Z. Yang, Y. Yu, J. Yang, *Nano Energy* **2018**, *46*, 20–28.
[33] Z. Zhao, W. Chen, S. Impeng, M. Li, R. Wang, Y. Liu, L. Zhang, L. Dong, J. Unruangsri, C. Peng, C. Wang, S. Namuangruk, S.-Y. Lee, Y. Wang, H. Lu, J. Guo, *J. Mater. Chem. A* **2020**, *8*, 3459–3467.
[34] G. Wang, C. Chen, Y. Chen, X. Kang, C. Yang, F. Wang, Y. Liu, X. Xiong, *Angew. Chem. Int. Ed.* **2020**, *132*, 2071–2076.
[35] Y.-C. Yin, Q. Wang, J.-T. Yang, F. Li, G. Zhang, C.-H. Jiang, H.-S. Mo, J.-S. Yao, K.-H. Wang, F. Zhou, H.-X. Ju, H.-B. Yao, *Nat. Commun.* **2020**, *11*, 1761.
[36] X. Shen, Y. Li, T. Qian, J. Liu, J. Zhou, C. Yan, J. B. Goodenough, *Nat. Commun.* **2019**, *10*, 900.
[37] C. Chang, Y. Yao, R. Li, Z. H. Guo, L. Li, C, Pan, W. Hu, X. Pu, *Nano Energy* **2022**, *93*, 106871.
[38] R.-M. Gao, H. Yang, C.-Y. Wang, H. Ye, F.-F. Cao, Z.-P. Guo, *Angew. Chem. Int. Ed.* **2021**, *60*, 2–8.
[39] K. R. Adair, C. Zhao, M. N. Banis, Y. Zhao, R. Li, M. Cai, X. Sun, *Angew. Chem. Int. Ed.* **2019**, *58*, 15797–15802.
[40] F. Liu, Q. Xiao, H. B. Wu, L. Shen, D. Xu, M. Cai, Y. Lu, *Adv. Energy Mater.* **2018**, *8*, 1701744.
[41] Y. Cui, S. Liu, D. Wang, X. Wang, X. Xia, C. Gu, J. Tu, *Adv. Funct. Mater.* **2021**, *31*, 2006380.
[42] D. Chen, S. Huang, L. Zhong, S. Wang, M. Xiao, D. Han, Y. Meng, *Adv. Funct. Mater.* **2020**, *30*, 1907717.
[43] Y. Lu, Y. Lu, C. Jin, R. Gao, B. Liu, Y. Huang, Y. Yu, J. Ren, Y. Deng, X. Tao, J. Lyu, *ACS Energy Lett.* **2021**, *6*, 2103–2110.
[44] H. Zhang, X. Liao, Y. Guan, Y. Xiang, M. Li, W. Zhang, X. Zhu, H. Ming, L. Lu, J. Qiu, Y. Huang, G. Gao, Y. Yang, L. Mai, Y. Zhao, H. Zhang, *Nat. Commun.* **2018**, *9*, 3729.
[45] S. Li, J. Huang, Y. Cui, S. Liu, Z, Chen, W, Huang, C, Li, R. Liu, R. Fu, D. Wu, *Nat. Nanotech.* **2022**, *17*, 613–621.

[46] Y. Wang, F. Liu, G. Fan, X. Qiu, J. Liu, Z. Yan, K. Zhang, F. Cheng, J. Chen, *J. Am. Chem. Soc.* **2021**, *143*, 2829–2837.
[47] Z. Wang, F. Qi, L. Yin, Y. Shi, C. Sun, B. An, H.-M. Cheng, F. Li, *Adv. Energy Mater.* **2020**, *10*, 1903843.
[48] S. Li, W. Zhang, Q. Wu, L. Fan, X. Wang, X. Wang, Z. Shen, Y. He, Y. Lu, *Angew. Chem. Int. Ed.* **2020**, *59*, 14935–14941.
[49] Y. Wang, S.-W. Ke, G. Qiao, J. Liang, X. Zhou, X. Song, Z. Tie, S. Yuan, J.-L. Zuo, Z. Jin, *Adv. Energy Mater.* **2024**, *14*, 2303051.
[50] H. Zheng, H. Xiang, F. Jiang, Y. Liu, Y. Sun, X. Liang, Y. Feng, Y. Yu, *Adv. Energy Mater.* **2020**, *10*, 2001440.

Manuscript received: April 13, 2025
Revised manuscript received: May 23, 2025
Accepted manuscript online: June 23, 2025
Version of record online: ■■, ■■

Research Article

Lithium Metal Batteries

Y. Wang, P.-C. Zhao, J. Sun, J. Liang, T. Shen, C.-H. Li*, Z. Jin* — **e202508224**

Titanium–Polyoxometalate Crosslinked Metallo–Supramolecular Polymer as Artificial Interfacial Layer for Highly Persistent and Low–Temperature Tolerant Lithium Metal Batteries

An advanced metallo-supramolecular polymer is designed and synthesized by utilizing a titanium–polyoxometalate (Ti-POM) to bridge organic and inorganic moieties, and it is utilized as an anodic interfacial protective layer (MSP-IPL) to stabilize lithium metal anodes. The MSP-IPL possesses superior ion-transfer ability and outstanding electrochemical/ambient stability. The uniformly distributed Ti-POMs can effectively bind with PF_6^-, enhancing Li^+ transference number ($t_{Li}^+ = 0.607$), promoting uniform distribution of Li^+ flux.